

Understanding Disorder, Vibronic Structure, and Delocalization in Electronically Coupled Dimers on DNA Duplexes

Brian S. Rolczynski, Sebastián A. Díaz, Young C. Kim, Igor L. Medintz, Paul D. Cunningham, and Joseph S. Melinger*



Cite This: <https://doi.org/10.1021/acs.jpca.1c07205>



Read Online

ACCESS |



Metrics & More

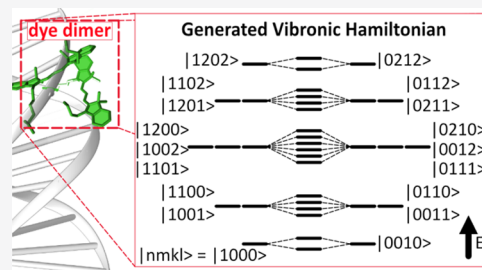


Article Recommendations



Supporting Information

ABSTRACT: Structural DNA nanotechnology is a promising approach to create chromophore networks with modular structures and Hamiltonians to control the material's functions. The functional behaviors of these systems depend on the interactions of the chromophores' vibronic states, as well as interactions with their environment. To optimize their functions, it is necessary to characterize the chromophore network's structural and energetic properties, including the electronic delocalization in some cases. In this study, parameters of interest are deduced in DNA-scaffolded Cyanine 3 and Cyanine 5 dimers. The methods include steady-state optical measurements, physical modeling, and a genetic algorithm approach. The parameters include the chromophore network's vibronic Hamiltonian, molecular positions, transition dipole orientations, and environmentally induced energy broadening. Additionally, the study uses temperature-dependent optical measurements to characterize the spectral broadening further. These combined results reveal the quantum mechanical delocalization, which is important for functions like coherent energy transport and quantum information applications.



INTRODUCTION

Nature has overcome complex challenges, such as photosynthesis and solar water oxidation,^{1,2} using organic chromophore networks scaffolded by proteins. Analogously, organic molecules can be templated onto DNA scaffolds with nanoscale accuracy^{3–5} and, in some cases, orientational control.^{5,6} As a result, applications have been proposed for DNA-scaffolded dye networks, such as light harvesters⁷ and quantum gates.^{3,8} The properties of these scaffolded systems can be very sensitive to the chemical structure, and sometimes even the presence of one or two atoms can rewrite their dynamics and functions.^{9,10} Nonetheless, applications like these could benefit from coherent processes if they were well optimized,¹¹ though examples in biology are subject to the fragility of coherent states in organic systems.^{12,13} Disruptions to the electronic delocalization and coherence occur through sources of disorder, like static inhomogeneities and dynamic structural motions, leading to effects like localization and dephasing.^{14,15} Low-frequency intramolecular vibrational modes contribute most significantly to dephasing in organic aggregates due to the transient disorder they induce in the electronic energy levels.¹³

Despite these challenges in organic chromophore networks, particular molecular aggregates were reported to support excitons delocalized across hundreds of molecules.^{16,17} Furthermore, protein scaffolds were reported to tune the transient disorder and its dephasing effects, which are responsible for transient excitonic localization.^{18–20} However, some protein scaffolds do not have much effect.²¹ It is not yet

known whether DNA-scaffolded chromophore networks yield significant delocalization as well. However, before considering extended systems, first it is necessary to understand these effects in smaller scaffolded systems.

For this study, Cyanine 3 (Cy3) and Cyanine 5 (Cy5) dyes were chosen for their relatively strong peak molar absorption coefficients (1.5×10^5 and 2.5×10^5 M⁻¹ cm⁻¹, respectively) and large transition dipole moments (12.8²² and 13.4 D,²³ respectively), as well as for their well-known spectral signatures on DNA scaffolds that have been described experimentally and computationally.^{22,24–26} Cyanine dyes are also popular fluorescent labels for biological imaging. In part, this popularity is due to the tunability of their absorption and fluorescence peak maxima by the chemical modification of their polymethine or aromatic moieties.²⁷

This study has several aims. First, it analyzes the spectral peak-shifting characteristics as a function of temperature and discusses nonradiative decay effects that occur as a function of temperature in the scaffolded Cy5 dimers. Second, it describes the extent of vibronic delocalization in the DNA-scaffolded dimer systems. Third, it compares the photophysical character-

Received: August 13, 2021

Revised: October 12, 2021

istics of DNA-scaffolded aggregates to those of other previously published aggregated chromophore networks. And fourth, it describes a genetic algorithm approach to extract the positions, orientations, energy levels, and spectral broadening characteristics from steady-state optical measurements. Because of their chemical modularity and relatively controllable aggregation structures, DNA-scaffolded chromophore networks are a good fit for a genetic algorithm approach. For this analysis, this study examines the temperature-dependent linear absorption, excitation, and fluorescence spectra of DNA-scaffolded Cy3 and Cy5 monomers and dimers over a temperature range between 78 and 298 K. By using genetic algorithms to compare the measured and calculated spectra, the molecular positions, orientations, vibronic Hamiltonians, and energetic disorder are generated. The energetic disorder in the cyanine dimers is deduced by comparing the measured and calculated linear absorption and circular dichroism spectra and by examining temperature-dependent spectral measurements. These results are used to describe the system's vibronic delocalization through its inverse participation ratios,²⁸ determine the spectral broadening contributions, and glean the roles of temperature, solvent, and interchromophore interactions on these parameters.

METHODS

Sample Preparation. DNA strands that were labeled with Cy3 or Cy5 dyes were obtained from Integrated DNA Technologies (Coralville, IA). They were purified using high-performance liquid chromatography. All DNA strands were rehydrated with ultrapure water to produce stock solutions at a concentration of 100 μM . DNA duplexes containing Cy3 or Cy5 monomers, or their homogeneous dimers, were prepared in a 2.5 \times phosphate-buffered saline buffer (PBS; 342.4 mM NaCl, 25 mM phosphate, and 6.75 mM KCl) by combining the constituent DNA strands at a concentration of 25 μM (in each DNA strand) and thermally annealing the solution from 95 to 4 $^{\circ}\text{C}$ at 1 $^{\circ}\text{C}/\text{min}$. Higher ionic strength buffers like PBS are generally used to shield DNA's charges and optimize the formation efficiency. This effect is not vital when the structures are based on simple double-stranded DNA, but for the sake of eventual direct comparison with more complex structures that would require this stabilization, it was used here as well. The final pH was adjusted to 7.4 with HCl and NaOH, as required. See Section 1 and Figure S1 in the Supporting Information for the strand sequences and a discussion on sample purity. The solutions were used without further purification. In addition to the standard PBS buffer solution, cyanine homogeneous dimers were also prepared in a 2:1 glycerol/water mixture containing 2.5 \times PBS, which yield an optical-quality glass at cryogenic temperatures and resist cryodamage.^{29,30} Working stock solutions were prepared at double-stranded DNA concentrations of 2 μM and diluted as necessary. For the dimers, the Cy3 or Cy5 dyes appear in the same comparative positions on the complementary strands within the DNA duplexes.

Optical Spectroscopy. Steady-state absorption spectra at room temperature were recorded for 150 μL samples in a 1 cm pathlength cuvette using an Agilent 8453 diode array UV–vis spectrophotometer at a concentration of 2 μM in double-stranded DNA. For low-temperature measurements at 78 K, absorption spectra were recorded using a PerkinElmer Lambda 750 spectrophotometer. These measurements were obtained in a 1 mm pathlength quartz absorption cell mounted in a copper

sample holder that was attached to the cold finger of a Janis ST-100 cryostat. Circular dichroism (CD) measurements were performed at room temperature using a JASCO J-1500 CD spectrophotometer. The samples were placed in a 1 cm pathlength quartz cuvette (150 μL volume) at a concentration of 2 μM in double-stranded DNA.

Steady-state fluorescence spectra and fluorescence excitation spectra were measured using a Fluoromax-3 spectrofluorometer (Horiba Scientific). These measurements were corrected for the response of the lamp, grating, and detector. The excitation and emission slits were set to 2 nm unless specified otherwise. For temperature-dependent fluorescence measurements, the samples were loaded in a 1 mm pathlength cryogenic quartz cell (FireflySci) and mounted on a Janis STVP-100 sample-in-vapor cryostat. Liquid nitrogen was used as the cryogen, and the sample temperature was measured using a model 331 temperature controller (Lake Shore Cryogenics). The sample concentration for the fluorescence measurements was between 0.5 and 1.0 μM in double-stranded DNA, keeping the peak optical density below 0.1. Unless otherwise stated, for the Cy3 dimer fluorescence, excitation and emission frequencies were 19,417 cm^{-1} (515 nm) and 16,667 cm^{-1} (600 nm), respectively. Likewise, for the Cy5 dimer, these frequencies were 16,529 cm^{-1} (605 nm) and 13,699 cm^{-1} (730 nm), respectively.

Time-resolved fluorescence measurements were performed using time-correlated single-photon counting (TCSPC). Cyanine dimer samples were placed in 1 mm pathlength quartz cells at a peak optical density of $\lesssim 0.1$ and mounted on the Janis ST-100 cryostat, as described above. For Cy3 dimers, the excitation source was an 80 MHz repetition laser (High Q) producing 8 ps pulses at 532 nm. For Cy5 dimers, the excitation source was a home-built synchronously pumped and cavity-dumped dye laser producing 2 ps pulses near 600 nm at a repetition rate of 4 MHz. Photons were collected at the magic angle from the excitation polarization and detected using a thermoelectrically cooled microchannel plate photomultiplier (Hamamatsu R3809) mounted to the exit port of a monochromator. For Cy3, the detection frequency was 17,390 cm^{-1} (575 nm), and for Cy5, the detection frequency was 14,815 cm^{-1} (675 nm). Time-resolved fluorescence signals were recorded using a Becker & Hickl SPC-630 TCSPC card. The instrument response function was determined for each excitation frequency using a scattering solution and it was typically between 30 and 40 ps full width at half maximum.

Spectral Modeling. Hamiltonian. The following model describes the calculation of linear absorption and CD spectra for a monomer or dimer system. This model simulates the spectra based on a vibronic Hamiltonian^{25,31–36} in the presence of environmental (“bath”) perturbations. No electronic structure properties were simulated in this study; rather, the Hamiltonian elements were obtained by comparison of the computed and measured spectra.

In the Hamiltonian used here, one bright electronic excited state per chromophore was included. The Hamiltonian corresponding to the monomer \hat{H}^{mono} is shown in eq 1. For the electronic monomer state $|n\rangle$ and the corresponding vibrational state $|m\rangle$, the monomer's vibronic states are $|n, m\rangle = |n\rangle|m\rangle$. The diagonal elements of the Hamiltonian correspond to the excited-state energies $E_{n,m}$. For the calculations discussed in this study, only the first three vibrational levels corresponding to a single vibrational mode were included. This limitation has been made in similar

models³⁷ and is justified in the Results and Discussion section by the good match of the calculated and measured monomer spectra. As a result, the monomer Hamiltonian contained three diagonal elements, corresponding to the vibrational levels within the single excited electronic state.

$$\hat{H}^{\text{mono}} = \begin{bmatrix} E_{1,0} & \cdots & 0 \\ \vdots & \ddots & \vdots \\ 0 & \cdots & E_{N,M} \end{bmatrix} \quad (1)$$

Meanwhile, the dimer system Hamiltonian \hat{H}^{dimer} is described by eq 2. The states are $|n, m, k, l\rangle = |n, m\rangle|k, l\rangle$ for a dimer system with the molecules in states $|n, m\rangle$ and $|k, l\rangle$. However, these $|n, m, k, l\rangle$ states are no longer necessarily eigenstates of the dimer Hamiltonian because the intermolecular vibronic coupling elements can be nonzero. The diagonal elements contain energies $E_{n, m, k, l}$ corresponding to basis states where exactly one site's electronic state is excited though both may be vibrationally excited. For $E_{n, m, k, l}$ exactly one of n and k is equal to 0. The number of diagonal elements in the dimer Hamiltonian scales as NM^N , where N and M are the total number of electronic states and vibrational sublevels, respectively. For example, a dimer Hamiltonian that includes three vibrational sublevels has 18 diagonal elements.

$$\hat{H}^{\text{dimer}} = \begin{bmatrix} E_{1,0,0,0} & \cdots & 0 & V_{1,0,1,0} & \cdots & V_{1,0,K,L} \\ \vdots & \ddots & \vdots & \vdots & \ddots & \vdots \\ 0 & \cdots & E_{N,M,0,L} & V_{N,M,1,0} & \cdots & V_{N,M,K,L} \\ V_{1,0,1,0} & \cdots & V_{N,M,1,0} & E_{0,0,1,0} & \cdots & 0 \\ \vdots & \ddots & \vdots & \vdots & \ddots & \vdots \\ V_{1,0,K,L} & \cdots & V_{N,M,K,L} & 0 & \cdots & E_{0,M,K,L} \end{bmatrix} \quad (2)$$

The coupling elements are determined by eq 3.

$$V_{n,m,k,l} = F_{v,m} F_{v,l} C_{n,k} \left[\sum_{\alpha=0}^A \frac{1}{|r_{\alpha}^{+} - r_{\alpha}^{-}|} - \sum_{\beta \neq \alpha}^B \frac{1}{|r_{\alpha}^{+} - r_{\beta}^{-}|} \right] \quad (3)$$

The Coulombic couplings $C_{n,k}$ are determined by Coulomb's law interactions (eq 4) between these point charges for chromophores at sites α and β , up to the total number of states A and B, respectively.^{24,38} In eq 4, ϵ_{00} is the permittivity of free space. Here, r_{α}^{+} and r_{α}^{-} are the positive and negative partial charges' positions, respectively, on site α , and S is the Huang–Rhys factor. $F_{v,m}$ are the Franck–Condon factors (eq 5) for the vibrational state overlap between the ground-state vibrational level v (approximated to be 0 in this study) and the excited-state vibrational state associated with $|n, m\rangle$.²⁵ In eq 5, δ is the Dirac delta function. Huang–Rhys factors are estimated using eq 6 based on the experimentally determined Stokes shift γ and the estimated vibrational energy-level spacing ΔE_v^{est} . ΔE_v^{est} is estimated by a multiple Gaussian fit of the absorption spectrum. Subsequently, an additive term z is further optimized to accurately reproduce the peak heights in the monomer's linear absorption spectrum. These further optimizations are needed because the Stokes shift method is only accurate to $|z| \leq 0.25$,³⁹ so z is restricted to this range.

$$C_{n,k} = \frac{q_n q_k}{4\pi\epsilon_0} \quad (4)$$

$$F_{v,m} = \exp\left(\frac{-S}{2}\right) \sum_{\eta=0}^v \sum_{\xi=0}^m \frac{(-1)^{\xi}}{\eta! \xi!} \sqrt{\frac{S^{(\eta+1)} v! m!}{(v-\eta)! (m-\xi)!}} \delta_{(v-\eta)-(m-\xi)} \quad (5)$$

$$S = \left(\frac{\gamma}{2\Delta E_v^{\text{est}}} + \frac{1}{4} \right) + z \quad (6)$$

The chromophores within the dimer systems in this study are usually within close proximity, often less than one molecular length apart. Due to this close proximity, we do not use the point-dipole approximation. Instead, we use the extended dipole approximation, which is better because it has a $1/r$ dependence at short distances but reduces to the point-dipole approximation ($1/r^3$ dependence) at long distances. In practice, it was found to give superior results to the point-dipole approximation at close distances and equivalent results at larger distances.³⁸ The extended dipole approximation was found to be valid when the chromophores' transition dipole strengths were sufficiently large (>4 D), so that the dipolar interactions dominate the higher-order multipolar contributions even at short distances.³⁸ The systems discussed in this study meet this requirement. In the extended dipole approximation, two oppositely charged point charges are simulated on each monomer, on each end of the chromophore along the direction of its transition dipole.²⁴ For longer systems such as polymers, an effective coherence length would need to be set; however, the monomers used here are individually only 1–2 nm long, which is within the typical coherence lengths for organic systems.¹³ Therefore, the present model assumes that the transition dipole spans the entire length of each molecule. Within this model, the partial-charge magnitude q_n is determined by eq 7, where e is the elementary charge, μ_n is the transition dipole norm, and L_n is the molecular length along its longest conjugated dimension. The Cy3 and Cy5 monomer lengths are 15.3 and 16.1 Å, respectively, across the longest conjugated dimension. These lengths (L_n) were obtained by energy optimization using the Generalized Amber Force Field in the Avogadro program.⁴⁰

$$q_n = \frac{e\mu_n}{L_n} \quad (7)$$

Spectral Broadening. The model uses a correlation function approach⁴¹ that treats the bath effects as a perturbation on the vibronic states. In a multimode harmonic oscillator approximation for the nuclear bath's vibrational modes, the line shape function $g(t)$ is described in the time domain by eq 8.⁴¹

$$g(t) = \sum_j \Xi_j(\omega) \left[(1 - \cos(\omega_j t)) \coth\left(\frac{\beta \hbar \omega_j}{2}\right) + i(\sin(\omega_j t) - \omega_j t) \right] \quad (8)$$

In eq 8, ω_j and Ξ_j are the frequency and corresponding Ohmic spectral density magnitudes, respectively, for bath vibrational mode j . The scalar factor $\Xi_j(\omega)$ is shown in eq 9, where ω_c is the cutoff frequency and λ is the reorganization energy. We assume 200 cm⁻¹ for the cutoff frequency.

$$\Xi_j(\omega) = \frac{\lambda}{\omega_c} \exp\left(-\frac{\omega}{\omega_c}\right) \quad (9)$$

This study distinguishes the dynamic and static broadening contributions to the spectra. The dynamic contributions are those that can be explained by eq 8. The static contributions are due to the differences in the local environment or nuclear arrangement across the sample ensemble, which either do not vary on average or vary so slowly that they are effectively unchanging within the relevant time scales for the spectral measurement. These contributions are obtained by optimizing the linewidth of a Gaussian function convoluted to the calculated spectral peaks. These Gaussian linewidths are assumed to be equal for all peaks within a spectrum and for all the corresponding monomer and dimer spectra.

Oscillator and Rotational Strengths. After the system interacts with light, it emits a time-domain signal $q(t)$ (eq 10) with eigenenergy ω_α and line shape function $g_\alpha(t)$ for each eigenstate α (of A total eigenstates). The term P_α represents the oscillator strength P_α^{osc} (eq 11) or rotational strength P_α^{rot} (eq 12) for the linear absorption or CD spectra, respectively.

$$q(t) = \sum_{\alpha}^A P_{\alpha} \exp[-i\omega_{\alpha}t - g_{\alpha}(t)] \quad (10)$$

The oscillator or rotational strengths determine the peak heights within the linear absorption or CD spectra, respectively.⁴² Here, μ_a is the transition dipole and F_a are the Franck–Condon factors associated with the Hamiltonian's α^{th} eigenstate, while a and b refer to these parameters in the vibronic site basis. F_a are the Franck–Condon factors for the nuclear overlap between the ground-state vibrational level ν within the ground state (assumed to be 0 in this case) and the excited-state vibrational state associated with $|n, m\rangle$ or $|k, l\rangle$, whichever is electronically excited in state α (eq 10). Additionally, $r_{a,b}$ is the distance between sites a and b , and $c_{a,\alpha}$ is the overlap between the vibronic state a and the α^{th} eigenstate. The angular brackets indicate expectation values with respect to energy disorder, which is estimated using a Gaussian convolution. This energy disorder is due to inhomogeneities in the sample ensemble, such as rotations about single bonds, which can perturb the energy levels. Equation 12 applies to dimers only; the monomers have no optical CD signal. In eqs 11 and 12, coefficients such as Planck's constant and the speed of light⁴³ have been omitted by convention.⁴² In fact, the oscillator and rotational strengths are dimensionless.

$$P_{\alpha}^{\text{osc}} = \langle |F_{\alpha} \mu_{\alpha}|^2 \rangle \quad (11)$$

$$P_{\alpha}^{\text{rot}} = \left\langle \sum_a \sum_{b>a} c_{a,\alpha} c_{b,\alpha} F_a F_b (r_{a,b} \cdot (\mu_a \times \mu_b)) \right\rangle \quad (12)$$

Genetic Algorithm. The purpose of this approach is to find the optimal set of sample parameters which results in the calculated spectra that are the best simultaneous match to the measured absorption and CD spectra. The genetic algorithm performs this optimization stochastically. In overview, given the initial sets of guess parameters, the genetic algorithm continually splices and resplices the most optimal parameter sets together until no better-scoring one can be found.⁴⁴ During this process, random mutations are introduced to expand the search space. These mutations change the values of

particular numbers within the parameter sets according to a Gaussian distribution. In the process, the algorithm also performs niching procedures, which resist local optima. Here, niching techniques are used, such as clearing and Delaunay triangulation.⁴⁵ Clearing operations delete nearly identical parameter sets, so that small regions of the search space do not become overrepresented in the ensemble. Delaunay triangulation is used to reassign these deleted sets to empty regions of the search space. Finally, genetic algorithms benefit from a gradually reducing search scope. Initially, large random mutations are used to perform a coarse search of the parameter space, while the mutations in subsequent iterations have smaller standard deviations to perform a fine search.

Figure 1 presents an overview of the genetic algorithm procedure. A set of initial parameters is supplied to the

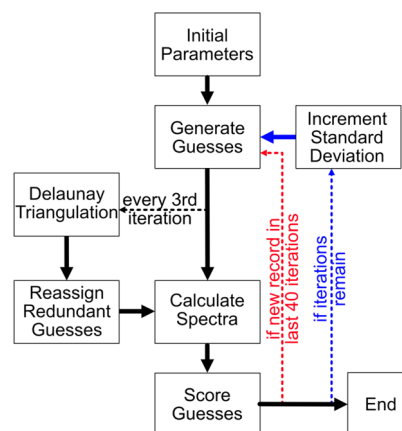


Figure 1. Flow chart of the genetic algorithm. The algorithm starts at the initial parameters box. Solid arrows represent the main path, while dotted arrows represent if statements that take precedence if the listed condition is true. The “Increment Standard Deviation” box refers to incrementing the width of the standard deviation used for random perturbations of the guesses.

algorithm, which is used to generate 200 sets of guess parameters. After these sets of guesses are generated, they are used to calculate the linear absorption and CD spectra. The spectra are scored using a method described subsequently. Based on the scores, the individuals within the ensemble are selected, and occasionally randomly mutated, and then merged to generate the next generation of 200 guess sets.

The initial parameter sets assign the following variables for each monomer: transition dipole orientations, electronic and vibrational energy spacings, Cartesian coordinates, and Gaussian static linewidth broadening. Because homogeneous dimers are used in this study, the energy levels and linewidth parameters are assumed to be identical for each monomer within the dimer. To generate the initial guess sets, the first monomer is always oriented along the z -axis and its position is set to the origin. For the second monomer, transition dipole orientations are initially generated by systematically sampling the inclination (θ) and azimuthal (φ) angles. These angles are restricted to ranges of $0-\pi$ and $0-2\pi$, respectively. Standard deviations to determine the Gaussian linewidths are systematically generated in a range of approximately $200-500 \text{ cm}^{-1}$ with a constant step size, and an assumption is made that all spectral peaks have the same linewidth. The energy and position terms from the input parameters are randomly varied for each generated guess. The energy terms were restricted to a

range that encompasses the spectra, which for Cy3 and Cy5 was 16,000–23,000 cm^{-1} and 14,000–19,000 cm^{-1} , respectively.

In subsequent generations, the ensemble of guess sets is generated by selecting and merging guess sets from the previous generation, but new values are also introduced by random mutations. The mutations are performed by reassigning parameters of randomly selected guess sets using a Gaussian distribution with a varying standard deviation. Earlier iterations use a larger standard deviation to perform coarse optimization, while subsequent generations use a smaller standard deviation to more finely tune the parameters. As the algorithm progresses, systematically smaller Gaussian standard deviations (σ) are used for these mutations, advancing whenever no higher-scoring individual was produced for 40 iterations in a row. For this study, these standard deviations were 500, 100, 10, 3, 1, 0.4, 0.1, 0.01, and 0.001. Incrementation of the standard deviation from this list is referred to in the “Increment Standard Deviation” box in Figure 1.

To score the guesses, the calculated spectra were compared to the corresponding experimentally measured linear absorption and (if not a monomer) CD spectra as well as their first derivatives. Within each generation, the k^{th} guess set was scored according to the cost function F_k (eq 13). Here, $f_{k,i}$ are the summed difference square between the calculated and experimental spectra and i refers to absorption, CD, and their respective derivatives ($i = 1-4$, respectively). In this equation, the summed terms tabulated the differences between the spectra, and the product terms were empirically determined to prevent the algorithm from sacrificing lower-scoring spectra entirely to better fit higher-scoring ones. The result was a balanced scoring outcome that optimized all of the spectra simultaneously.

$$F_k = \left(\frac{1}{\prod_{i=1}^4 f_{k,i}} \right) \left(\sum_{i=1}^4 \frac{1}{f_{k,i}} \right) \quad (13)$$

To generate the next generation of guess sets, the highest-scoring set was conserved without alteration, and then the remaining guess sets were generated using pairs of guess sets from the previous generation. The pairs were selected using a probability function $P(k)$ (eq 14). The selections were performed with replacement, so that the same guess set could be chosen more than once.

$$P(k) = \frac{F_k}{\sum_{j=1}^{200} F_j} \quad (14)$$

The next generation's guess sets were assigned values from either of the two parents with equal probability, determined independently for each element.

In practice, this algorithm tended to cause the guesses to converge to local optima. This convergence wastes computational resources by making many of the guesses redundantly search the same region of the combination space. To address this problem, multimodal searching was implemented by using a clearing technique based on Delaunay triangulation.⁴⁵ Multimodal searching is a niching protocol that preserves the diversity of the population, typically by deleting or reassigning redundant guess sets. In a genetic algorithm, a basic clearing technique saves the highest-scoring unique guess sets, while it deletes slightly lower-scoring, nearly identical guess sets. This

process preserves multimodal searching; however it reduces the number of members in a given generation and therefore reduces the search efficiency. In the method we employ, rather than deleting these members, they are instead randomly reassigned to empty regions of the search space. To ensure that they are not assigned to occupied regions, the empty regions of the search space are calculated using Delaunay triangulation according to the following reference.⁴⁵

To reduce the computational cost, we employed three strategies: (a) the number of uncleared members included in the Delaunay triangulation was limited to 100, in the order of descending score; (b) Delaunay triangulation and reassignment were only performed on every third iteration of the genetic algorithm; and (c) four degrees of freedom were considered at a time per iteration (e.g., a particular orientation or energy parameter), which were randomly chosen for each iteration. The reassignment threshold was 30 individuals within a critical distance of 10^{-10} , which is effectively intended to reassign approximate duplicates only. This distance within the search space was calculated using the distance formula on the four parameters selected for each iteration.

RESULTS AND DISCUSSION

Deducing Chromophore Parameters from the Optical Spectra. The Cy3 and Cy5 chromophores used in this study are shown in Figure 2a. Cy5 has one additional double bond in its methine bridge, compared to Cy3. Other than this difference, the chemical structures are identical. The dyes attach to the DNA's phosphate groups by two propyl linkers, occupying the positions of DNA nucleotides (Section 1 of the Supporting Information). These linkers are intentionally short as longer linkers would invite increased nuclear motions that introduce disorder and strengthen decoherence. In the dimer samples, the two chromophores are inserted in conjugate positions on each strand of the DNA duplex. Molecular dynamics (MD) simulations in previous studies indicate that in this configuration, the chromophores tend to interact with the base-stacking region of the DNA. MD simulations of similar Cy3²⁵ and Cy5⁴⁶ DNA–chromophore dimer complexes show representative structures. Figure 2b–d shows the measured linear absorption and fluorescence spectra for the Cy3 and Cy5 monomers and dimers and CD spectra for the Cy3 and Cy5 dimers. These spectra were measured at room temperature with the chromophore-scaffolded DNA structures in the glycerol buffer solution. Compared to Cy3, the larger π -conjugation length in Cy5 results in lower-frequency fluorescence and absorption peaks in both the monomer and dimer spectra. The nonzero CD spectra indicate coupling between the dye molecules. The dimer spectra show Davydov splitting in the bands, including J-like and H-like bands that are red- or blue-shifted, respectively, from the peak positions in their corresponding monomer spectra.⁴⁷ The Cy5 dimer shows an H-like band near 15,460 cm^{-1} in its linear absorption spectrum. For the Cy3 dimer, the equivalent H-like band appears as a blue shoulder compared to the monomer's 0–0 band. The peak molar absorptivity in the Cy3 dimer increases by a factor of approximately 1.85 compared to the Cy3 monomer, whereas the peak molar absorptivity of the Cy5 dimer increases by about 1.5 with respect to that of the Cy5 monomer.

These experimental spectra were compared to those calculated using the model discussed in the Methods Section. These calculations include the linear absorption spectra for the

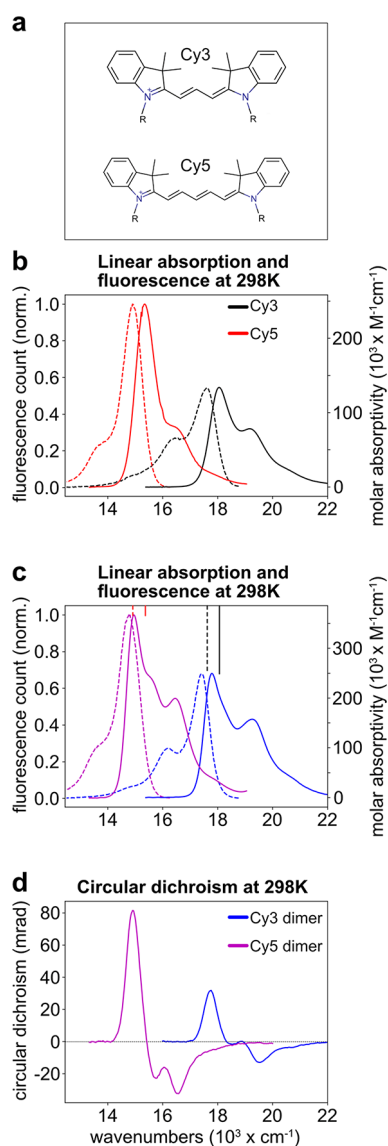


Figure 2. Spectra are shown for Cy3 and Cy5. The chemical structures are shown in (a). They represent one possible resonance structure because either nitrogen atom can be positively charged. The R-groups in this figure are propyl groups, which attach to the phosphate groups in DNA. When attached onto DNA, these dyes take the place of a nucleotide residue. The monomer (b) and dimer (c) fluorescence (dashed) and linear absorption (solid) spectra are shown as well as the dimer CD spectra (d). To aid in the comparison of the peak positions, the vertical lines on the top of panel (c) indicate the fluorescence (dashed) and linear absorption (solid) peak maxima for the monomers. In all cases, the dye–DNA structures are in glycerol buffer. All measurements were made at 298 K.

DNA-scaffolded monomers and dimers and the CD spectra for the dimers (Figure 3a–f). Table 1 shows the molecular parameters used to calculate the spectra obtained using the genetic algorithm described in the Methods Section (Table 1). Here, θ is the inclination angle; ϕ is the azimuthal angle; x , y , and z are Cartesian coordinates of the molecule's central position; E_{0-0} is the optical gap between the lowest vibrational modes in the ground state and the first excited state; ΔE_v is the vibrational spacing for the vibrational mode included in the vibronic bases; and HWHM is the wavenumber half width at half maximum for the static inhomogeneous

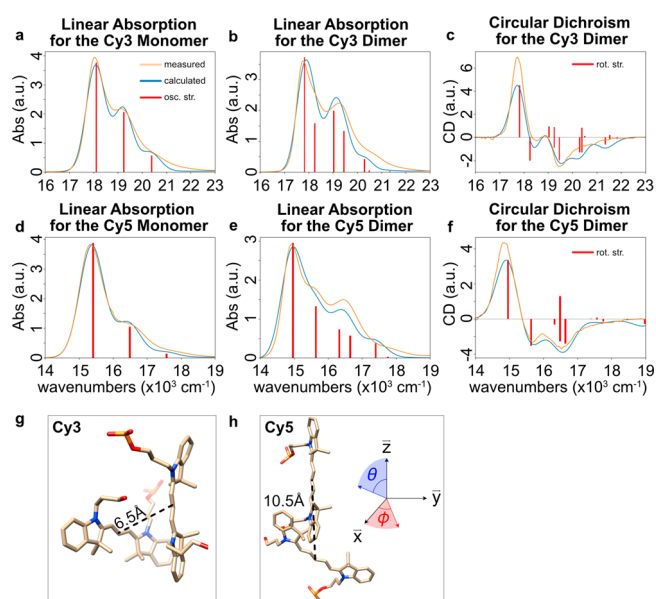


Figure 3. Measured and calculated linear absorption and CD spectra are shown for the Cy3 (a–c) and Cy5 (d–f) monomers and dimers at 298 K. The calculated spectra were optimized using a genetic algorithm as described in the Methods section. The corresponding parameters are shown in Table 1. Panels (g, h) show the structures of the Cy3 and Cy5 dimers obtained using the genetic algorithm, respectively. The oscillator or rotational strengths are shown as red bars, as indicated. In the physical model (eqs 11 and 12), these structures are ensemble averages. The energetic distribution across the ensemble is assumed to be Gaussian and quantified by the HWHM term, as shown in Table 1. More molecular images from different perspectives are shown in Figure S2 in the Supporting Information.

Table 1. Position, Transition Dipole Orientation, and Energy Parameters of the Second Site in the Cy3 and Cy5 Dimers^a

	Cy3	Cy5
θ (deg.)	99.3	104.6
ϕ (deg.)	8.27	87.4
x (Å)	−6.3	−2.9
y (Å)	−0.9	−4.6
z (Å)	−1.5	−9.0
E_{0-0} (cm^{-1})	18,104	15,412
ΔE_v (cm^{-1})	1144	1082
HWHM (cm^{-1})	126	135

^aFor comparison, the first site has its inclination angle (θ), azimuthal angle (ϕ), and position coordinates (x , y , z) set to zero, while the optical gap (E_{0-0}), vibrational spacing (ΔE_v), and peak-broadening HWHM are assumed to be equal for both sites. The HWHM is also assumed to be equal for all peaks within a spectrum.

component of the spectral linewidths. For the dimers, a convention is adopted that the first site's transition dipole has θ , ϕ , x , y , and z set to zero.

The average positions and orientations for the Cy3 and Cy5 dimers are shown in Figure 3g,h. Note that the model does not account for the possibility of multiple, highly distinct stable (or metastable) conformations and instead treats an average conformation with Gaussian energy deviations. Though not done here, in principle, the algorithm's cost function could be extended to consider multiple configurations at once if the present treatment could not effectively reproduce the spectra.

The coincidence of the measured and calculated linear absorption spectra suggests that the present treatment is sufficient for the systems studied here. The coincidence of the monomer spectra also confirms that the energy parameters are a good match for the isolated chromophore and that three vibrational levels must be included within each electronic state to produce a match of the experimental spectrum.

The Huang–Rhys factors were determined by analysis of the Stokes shifts (see the [Methods](#) section).³⁹ The Stokes shifts for Cy3 and Cy5 at room temperature were 385 and 296 cm^{-1} , respectively. However, the Huang–Rhys factors obtained from these Stokes shifts are only accurate to a range of $\pm \frac{1}{4}$.³⁹ To optimize the estimates, the values were optimized until the peak heights coincided for the calculated and measured monomer linear absorption spectra. As a result, the Huang–Rhys factors were determined to be $S_{\text{Cy3}} = 0.55$ and $S_{\text{Cy5}} = 0.27$.

Characterizing the Sources of Disorder. The disorder discussed here refers to the distribution of vibronic state energies within the sample population, which contributes to the line widths of the sample's spectroscopic peaks. This disorder arises from static and dynamic sources. Static sources are those that are effectively invariant compared to the signal's dephasing rates,⁴¹ such as some structural inhomogeneities, distinct local electrostatic fields, and chemical defects. In contrast, dynamic sources of disorder occur quickly enough to coincide with dephasing, and therefore, also the localization of vibronic superpositions. An example is stochastic perturbations of the vibronic states caused by rapid nuclear rearrangements.¹³ It is useful to distinguish these sources of disorder to provide direction for how to further optimize the system. If the goal is to use DNA-scaffolded systems for coherent quantum mechanical phenomena, for example, it is helpful to understand how much the individual chromophore motions are contributing to the decoherence and how much of the spectral broadening is due to ensemble-level effects like sample polydispersity. Here, these sources of disorder are parsed using the genetic algorithm results as well as the spectral temperature- and solvent-dependencies.

To characterize the sources of disorder in the DNA-scaffolded chromophore structures, we measured temperature-dependent fluorescence excitation and emission spectra for Cy3 and Cy5 dimers, as shown in [Figure 4](#) (for normalized spectra, see [Figure S3](#)). For the Cy3 dimers, both the excitation and emission spectra continuously narrow as the temperature is lowered to 78 K, especially in the region near the 0–0 transition (approximately 17,850 cm^{-1} ; see [Figure S4](#)). In addition, both the excitation and emission spectra undergo a blue shift as the temperature is lowered. In contrast, the Cy5 dimer exhibits red shifts for both the excitation and emission spectra as the temperature is initially lowered. Notably, the Cy5 dimer excitation spectrum near room temperature resembles that of the Cy5 monomer. As the temperature is lowered, the excitation spectrum evolves into a band shape with the coupled electronic features (as distinct from the monomer spectra) observed in the absorption spectrum ([Figure 4](#)). For both the Cy3 and Cy5 dimers, there is a strong increase in the fluorescence emission intensity as temperature is lowered, suggesting that relaxation processes that cause fluorescence quenching become suppressed at lower temperatures. This result is consistent with the previous report that a fast (<60 ps) nonradiative decay channel is deactivated in DNA-scaffolded Cy5 dimers as temperature decreases.⁴⁸ For

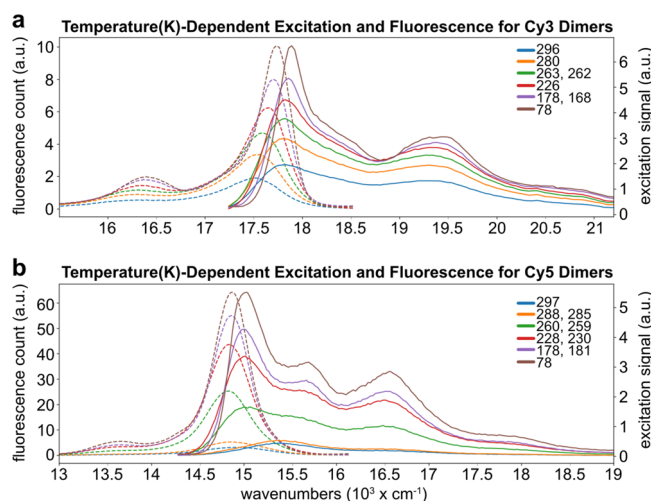


Figure 4. Measured temperature-dependent fluorescence (dashed) and excitation (solid) spectra are shown for the Cy3 (a) and Cy5 (b) dimers in glycerol buffer. The line colors indicate the temperature (K). A single number listed in the temperature legend indicates that the excitation and fluorescence had the same temperature. However, some of the spectra were measured at slightly different temperatures, as indicated in the color bar in the order of excitation, and fluorescence temperature.

comparison, [Figure S5](#) shows the temperature-dependent emission properties of DNA-scaffolded Cy3 and Cy5 monomers. The monomer emission spectra also exhibit line narrowing and blue shifting as the temperature is lowered to 78 K.

[Figure S6](#) shows the temperature-dependent integrated fluorescence yield and the excited-state lifetimes for Cy3 and Cy5 dimers. The vertical red lines indicate the approximate temperature where the sample formed a solid glass. This transition was typically accompanied by the formation of cracks in the solidified glass-like sample. The formation of the solid glass introduced some nonuniformity in the sample cell, which overlapped with the illumination footprint. Therefore, it was difficult to calibrate the integrated fluorescence from the sample at temperatures below the glass formation. Above the critical temperature for glass formation, it was possible to quantify the fluorescence increase. For the Cy3 dimer at approximately 175 K, a threefold increase in integrated fluorescence was found relative to room temperature. Considering that the fluorescence quantum yield is approximately 33% for the Cy3 dimer (in glycerol buffer) at room temperature, the quantum yield increases to nearly unity for temperatures below about 175 K.

This increase is explained by the deactivation of nonradiative relaxation pathways. [Figure S7a](#) shows that the Cy3 dimer fluorescence decay curve lengthens from an average lifetime of 1.4 ns at room temperature (assuming a biexponential decay) to a nearly single-exponential decay time of 2.6 ns. The Cy5 dimer (in glycerol buffer) showed an 11-fold increase for the integrated fluorescence intensity at approximately 175 K, relative to that measured at room temperature ([Figure S7b](#)). The fluorescence decay curve at room temperature contains approximately 80 ps, 700 ps, and 2 ns time constants when fit to a triexponential decay function. The first two of these time constants are associated with twisting or rotations about the single bonds in the cyanine dyes under differing steric constraints,^{49,50} indicating that the sample ensemble is subject

to a distribution of steric hindrances. This distribution is possible if there is a diversity of nuclear configurations involving dimer interactions.⁵¹ The 80 ps relaxation time is consistent with rapid internal conversion in the strongly coupled Cy5 dimers.⁵² Furthermore, the 700 ps component is consistent with the time constants of these structural rearrangements measured in cyanine chromophores under more extreme steric hindrance. In a previous study,⁵¹ bulky substituents provided this hindrance; however, in the present samples, it can be provided by the interaction of the two chromophores within the dimer and/or interactions between these chromophores and the DNA scaffold. Furthermore, cyanine systems with strong steric hindrance due to rotation about single bonds were reported with fluorescence decay rates of several nanoseconds.⁵⁰ Alternatively, the 700 ps or 2 ns components may be related to monomer species from defects (e.g., photobleaching products) and/or dimers with imperfect hybridization.

The 78 K Cy5 dimer emission spectrum (Figure 4) shows that the leading edge of the spectrum contains a small tail at the red edge near 650 nm. This feature may be due to emission from monomer-like species. To further examine this possibility, Figure S8 shows numerical superpositions of the measured 78 K Cy5 dimer and 78 K Cy5 monomer spectra containing up to 15% added Cy5 monomer to the experimental spectrum, which results in an increased amplitude in the tail on the blue side of the emission. Conversely, subtracting 7% of the Cy5 monomer from the experimental spectrum results in the leading edge of the dimer peak being well fit by a Gaussian function. This result coincides with an impurity analysis conducted using a PAGE gel (Figure S1), which resulted in an upper-bound estimate of approximately 8% double-stranded DNA dissociation.

At 78 K, the Cy5 dimer fluorescence decay curve lengthens to 2.5 ns and is nearly described by a single-exponential function. This observation is consistent with the dramatic lengthening of Cy5 dimer time constants observed in ultrafast pump–probe measurements of Cy5 dimers when cooled to 100 K.⁵³ The saturation of the integrated fluorescence from Cy5 dimers in Figure S6 shows that the excited-state relaxation channel is quenched at temperatures near 200 K, corresponding to an activation energy of approximately 140 cm^{−1}.

Figure 5 shows the temperature dependence of the 0–0 linewidth (HWHM) and peak frequency. The HWHM is used to describe the 0–0 band linewidth because the overlapping vibronic peaks limit visibility of the blue side of the peak (Figure S9). For the Cy3 monomer and dimer, the linewidth narrowed by approximately a factor of two at 78 K. In both cases, the fluorescence peaks blueshift and narrow. For the Cy5 monomer and dimer, the linewidth also narrows by approximately a factor of two at 78 K; however, as noted in Figure 4, the peak frequency for the dimer first redshifts until the temperature reaches about 260 K, whereupon the peak frequency reverses and gradually blueshifts as the temperature is lowered to 78 K. For both Cy3 and Cy5, the width of the dimer peaks is consistently narrower than the linewidth of the corresponding monomer due to an exchange-narrowing effect.⁵⁴ In the case of dimers, the rapid excitation energy exchange between the two sites has the effect of averaging over inhomogeneous site energies and can narrow the 0–0 dimer absorption (fluorescence) up to $\frac{1}{\sqrt{2}}$ the width of the monomer.

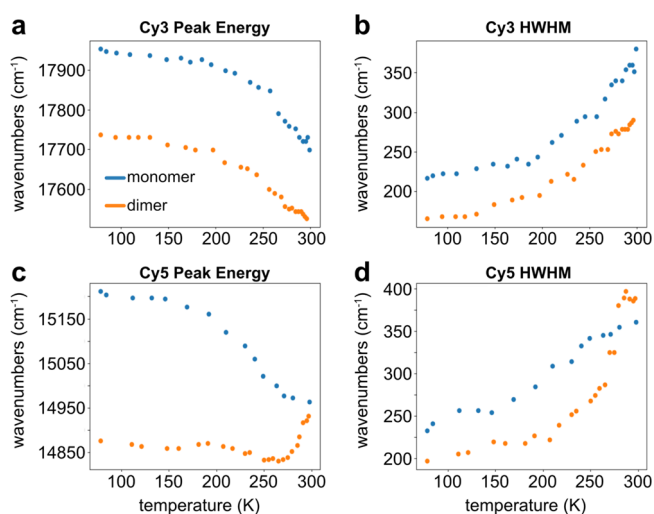


Figure 5. Temperature dependencies of the central peak energies and HWHM are shown for the measured fluorescence spectra as a function of temperature. For Cy3 (a, b) and Cy5 (c, d) dimers, the 0–0 peak energies (a, c) and HWHMs (b, d) are shown. The uncertainties in HWHM and peak energy are estimated to be ± 15 cm^{−1} for the Cy3 dimer and ± 11 cm^{−1} for the Cy5 dimer.

Figure 6 compares the linear absorption and fluorescence spectra of the Cy3 and Cy5 dimers at 78 K. The narrower

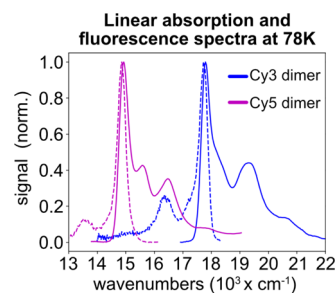


Figure 6. Measured fluorescence (dashed) and linear absorption (solid) spectra are shown for the dimers at 78 K. The samples were measured in a glycerol buffer mixture.

spectra can be explained by the system–environment coupling strength per unit time Δ^2 (eq 15). This term describes the energy-level perturbation magnitudes by interactions with an external vibrational environment, which cause the Hamiltonian's eigenvalues to fluctuate and introduce spectral broadening contributions to the time-integrated spectra. These effects depend on the temperature T and reorganization energy λ (eq 15).

$$\Delta^2 = \frac{2\lambda k_B T}{\hbar} \quad (15)$$

This coupling strength, which corresponds to the standard deviation of the Gaussian spectral peaks in the inhomogeneous broadening limit, decreases with temperature.⁴¹ At 78 K, the Cy3 and Cy5 dimers' Stokes shifts are 55 and 51 cm^{−1}, respectively. For reference, the dimers' shifts are smaller than the monomers' excitation shifts of 164 cm^{−1} for Cy3 and 165 cm^{−1} for Cy5 at 78 K (Figure S5e). This difference between the dimers and monomers at 78 K suggests that the chromophores within the dimer cause steric hindrance upon each other, which lowers their reorganization energy.

Compared to the previously studied chromophore networks, the Stokes shifts of the dimers are approximately two times larger than those observed in well-ordered J-aggregates,⁵⁵ and they are much smaller than the 600 cm^{-1} shift observed in disordered perylene bis-imide J-aggregates.⁵⁶

DNA-scaffolded systems have been observed to support vibronic coherences with decoherence time constants of 300 fs at room temperature,⁴⁶ which are similar to those observed in pigment–protein complexes.⁵⁷ These dynamics can involve both static and dynamic broadening (or equivalently, dephasing) contributions. The dynamic contributions occur when the environment's nuclear motions cause the system's vibronic energy levels to fluctuate. These dynamics are influenced by Δ^2 (eq 15). In the inhomogeneous limit, the reorganization energy can be estimated as half of the Stokes shift.³⁹ The Stokes shifts observed in the room-temperature spectra allow the estimation of 2λ . For the room-temperature monomer measurements, $\lambda_{\text{Cy3}} = 192 \text{ cm}^{-1}$ and $\lambda_{\text{Cy5}} = 148 \text{ cm}^{-1}$. For comparison, the Stokes shift for the Cy3 dimer sample at room temperature is 368 cm^{-1} , yielding a similar reorganization energy of 184 cm^{-1} . The Cy5 dimer's reorganization energy is not estimated using this method because its fluorescence appears to be monomer-like, so it is likely that the dimer fluorescence is significantly quenched. These values are similar to those found in bacteriochlorophyll *a*, which span 160–340 cm^{-1} depending on the choice of solvent.⁵⁸ Using these values, Cy3 and Cy5 yield Δ^2 values of 3.87 and 3.39 $\text{cm}^{-1} \text{ fs}^{-1}$, respectively.

The 0–0 peak widths are likely dominated by static broadening effects, such as sample polydispersity or differences in their local environments within the ensemble. For instance, previous measurements of the temperature-dependent homogeneous peak width of the 0–0 absorption line in pseudoisocyanine (PIC) J-aggregates were performed using the photon echo technique,⁵⁹ which can extract the dynamic homogeneously broadened signal even from a sample whose fluorescence and linear absorption measurements would be dominated by static inhomogeneous broadening.⁶⁰ In that work, the homogeneous linewidth was less than 5 cm^{-1} at temperatures near 78 K. Furthermore, Figure 5 shows that, as temperature decreases, the reduction in HWHM flattens out substantially by 78 K. In comparison, we achieve fluorescence 0–0 peak HWHM values no smaller than 162 nm even if the exit slit widths are reduced to 0.5 nm to minimize any instrument broadening effects (Figure S9). The difference in peak widths suggests that the 0–0 linewidths observed for Cy3 and Cy5 dimers at 78 K are dominated by static broadening. The genetic algorithm model (described previously) distinguishes both the dynamic and static homogeneous broadening components, and its outputs assign static inhomogeneous broadening HWHM contributions of 126 cm^{-1} (Cy3) and 135 cm^{-1} (Cy5). The algorithm uses the same value for both the monomers and dimers. These values comprise the majority of the observed peak widths and therefore support this assessment.

The fluorescence spectra of the Cy3 monomer and dimer exhibit monotonic redshifting and peak-broadening behaviors as the temperature increases (Figure 5). The Cy5 monomer and dimer spectra follow a similar pattern at lower temperatures, but aberrations occur as the temperature rises past a threshold of approximately 260 K. The Cy5 monomer's peak-shifting pattern differs from that of the Cy3 monomer by flattening out asymptotically toward 14,970 cm^{-1} as temper-

ature increases from 260 K to room temperature. Meanwhile, the Cy5 dimer's 0–0 peak blueshifts toward this same wavenumber value as the temperature increases past 260 K. However, at the same time, the excitation spectra (Figure 4) did not exhibit this abrupt change at 260 K. This mismatch in the excitation and fluorescence spectrum behaviors as the temperature is increased past 260 K suggests that different subensembles within the sample are responsible for the absorption and emission. Either multiple subensembles exist within the sample only at temperatures above 260 K, some of which dominate the absorption but not the fluorescence, or these subensembles exist at all temperatures, but certain ones in the dimer mixture become nonfluorescent at temperatures over 260 K. A previous study supports the latter explanation involving nonfluorescent subensembles.⁵²

Comparison to Other Organic Chromophore Networks. It is useful to compare the degree of inhomogeneous broadening in the cyanine dimer–DNA systems to inhomogeneous broadening found in other well-known organic aggregates. Here, the present results are compared to those of the thiocarbocyanine-triethylammonium salt (THIATS) J-aggregate⁵⁵ and perylene diimide (PDI) J-dimers.³⁵ The THIATS monomer is structurally similar to Cy3. The absorption and fluorescence spectral linewidths of the THIATS J-aggregate narrow to a HWHM linewidth of about 40 cm^{-1} near 78 K. This value is four times narrower than the HWHM reported here for the Cy3 dimer. However, the exciton coherence length for THIATS is estimated to extend over 20 molecules, implying a threefold greater exchange-narrowing effect compared to Cy3. Thus, the inhomogeneous broadening for the Cy3 dimer on DNA, while larger than for THIATS J-aggregates, is still within approximately a factor of two. In the case of the covalently formed PDI J-dimer, the HWHM's static inhomogeneous broadening contribution was determined to be $\sim 180 \text{ cm}^{-1}$ from single-molecule fluorescence measurements at 1.6 K where the dimer was dispersed in a host polymer matrix,³⁵ which is similar to the 200 cm^{-1} estimate for our Cy3 and Cy5 dimers on DNA obtained by using the peak width values in Figure S9 and multiplying by $\sqrt{2}$ to correct for the exchange-narrowing effect.

Sample Inhomogeneities. The excitation and emission spectra were measured at different detection and excitation frequencies, respectively, to characterize possible inhomogeneities in the dimer–DNA ensembles. Figure 7a shows that the excitation spectra for the Cy3 dimers show only small variations in the peak frequency as the detection wavenumber is varied from 18,349 to 19,417 cm^{-1} . There is a slight redshift of the edge of the 0–0 band over the same range of detection frequencies. The fluorescence emission spectra (Figure 7b) show equivalent peak wavenumbers and band shapes as the excitation frequencies is varied between 16,667 and 17,544 cm^{-1} . In the case of the Cy5 dimer, there is a greater dependence of the excitation spectrum on the detection wavenumber. For example, as the detection frequency is varied from 13,699 to 14,493 cm^{-1} , the peak frequency varies by approximately 150 cm^{-1} with a proportional redshift of the edge of the 0–0 band (Figure 7d). In addition, for detection at 14,085 cm^{-1} , the excitation spectrum shows a relative enhancement of both the bands near 15,500 and 16,525 cm^{-1} . Similar to the case of the Cy3 dimer, the Cy5 dimer emission spectra are relatively constant as the excitation frequency is tuned from 15,504 to 16,529 cm^{-1} (Figure 7c).

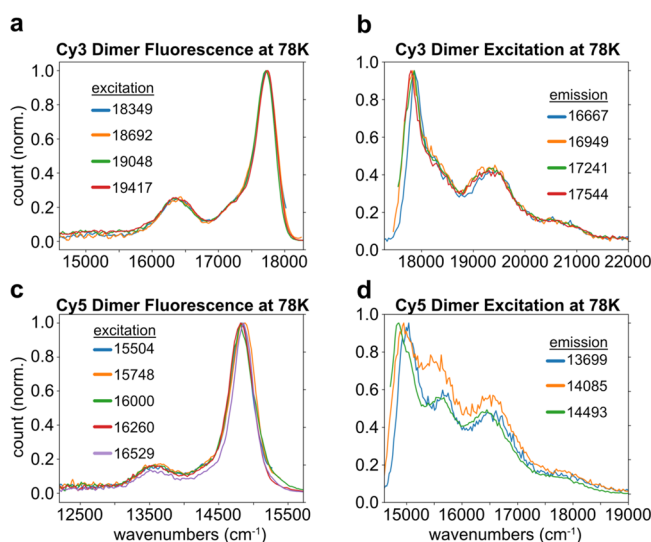


Figure 7. Normalized fluorescence (a, c) and excitation (b, d) spectra are shown for the Cy3 (a, b) and Cy5 (c, d) dimers measured at 78 K. For the fluorescence spectra, the color key indicates the excitation wavenumber, whereas the key in the excitation spectra indicate the detection wavenumber.

The variations in the Cy5 dimer excitation spectra that are not replicated in the fluorescence spectra suggest that the dimer ensembles contain subpopulations with different geometrical configurations of the chromophores and/or different local environments. The stronger variations in the Cy5 dimer excitation spectra suggest that this ensemble contains greater variation in dye configurations than does the ensemble of Cy3 dimers. One possible explanation is there may be increased strain in the local dye–DNA structure from the larger size of the Cy5 molecule that causes the Cy5 dimer configuration to be less robust than the Cy3 dimer configuration. The 0–0 fluorescence linewidths for the Cy3 and Cy5 dimers remain independent of the excitation frequency, which indicates that the subpopulations have similar inhomogeneous broadening. The wavenumber-dependent excitation spectra are consistent with MD simulations of Cy3 dimers and Cy5 dimers on DNA duplexes, which show that Cy3 and Cy5 dimers doubly attached to DNA duplexes tend to fluctuate between different dye orientations, though they have certain strongly dominant configurations.^{25,46}

The line-narrowing effect and fluorescence excitation and emission band shapes for the cyanine dimers on DNA depend on the solvent. The spectra shown in the previous figures have been measured in a glycerol–water buffer, which forms a fairly high-quality glass. Figure S10a–d shows the temperature-dependent excitation and emission spectra for the Cy5 dimer in PBS buffer without any glycerol. Here, the solution was observed to freeze near 260 K into a polycrystalline matrix. Under these conditions, the excitation and emission spectra do not narrow when cooled to 78 K. The spectra remain very broad with a 0–0 HWHM linewidth of approximately 370 cm^{-1} , which is nearly twice as large as the HWHM for the Cy5 dimer in the glycerol–water buffer at 78 K. In addition, Figure S10e shows that the Stokes shift at 78 K is 540 cm^{-1} , which is approximately 8 times larger than the Stokes shift observed in glycerol. These observations demonstrate that the crystallization of the solvent disrupts the orientation of the Cy5

dimers, which are held by relatively weak van der Waals interactions, creating a highly disordered ensemble of dimers.

Vibronic State Delocalization. The vibronic delocalization in the dimers will be discussed using the Hamiltonians obtained from the genetic algorithm. The vibronic basis states are themselves delocalized if at least one ground-state site is vibrationally excited. While the electronic excitation is localized to a particular site (see Methods Section), it can accompany nuclear distortions in neighboring sites.⁶¹ Aside from that kind of delocalization, any vibronic coupling in the Cy3 and Cy5 dimer Hamiltonians indicates delocalization among the vibronic excited states. In that case, the vibrons are no longer eigenstates of the system, and the eigenstates will delocalize among them. Only this delocalization among vibronic states is quantified by the inverse participation ratio.

The inverse participation ratio N_i describes the distribution of the Hamiltonian's eigenstates among its vibronic basis states (eq 16). This metric has been used previously to analyze the extent of excitonic delocalization in protein-scaffolded organic chromophore networks.²⁸ In eq 16, $U_{mi} = \langle n = 1, m | \Psi_i \rangle$ is the overlap between the vibronic state and the i^{th} eigenstate Ψ_i of the vibronic Hamiltonian. The lower limit of N_i is 1, which describes localization of the eigenstate on a single vibronic state. In contrast, the upper limit (equal to the total number of vibronic states) denotes evenly distributed delocalization across all the vibronic states.

$$N_i = \frac{1}{\sum_{m=1}^N (U_{mi})^4} \quad (16)$$

Based on the Hamiltonians obtained from the genetic algorithm (Tables S3 and S4), the eigenenergies and inverse participation ratios for Cy3 and Cy5 are given in Table 2. The three lowest-energy eigenstates are delocalized across approximately 2.2–4.7 vibronic states for both dimer systems, and the eigenstates of Cy5 are slightly more delocalized than those of Cy3. Conversely, Cy5's higher-energy eigenstates are more localized than those of Cy3. The relatively low inverse

Table 2. Cy3 and Cy5 Dimers' Vibronic Eigenstate Frequencies (ω) and Inverse Participation Ratios (N_i) Are Listed

Cy3		Cy5	
ω (cm^{-1})	N_i	ω (cm^{-1})	N_i
17,829	2.22	14,965	2.32
18,256	2.12	15,640	2.21
19,035	4.53	16,329	4.70
19,249	2.21	16,494	2.99
19,249	2.21	16,494	2.99
19,457	4.45	16,652	4.59
20,300	6.26	17,401	2.96
20,393	2.00	17,576	1.57
20,393	2.16	17,576	1.27
20,393	2.07	17,576	1.88
20,393	2.16	17,576	1.17
20,499	6.39	17,761	3.04
21,352	4.21	18,465	4.43
21,536	2.06	18,659	2.00
21,536	2.06	18,659	2.00
21,835	4.30	18,983	4.95
22,680	2.00	19,687	2.05
22,681	2.00	19,878	2.24

participation ratios compared to the theoretical maximum of 18 indicate room for improvement. Greater delocalization bolsters applications such as quantum information technologies^{62–64} and, in concert with decoherence mechanisms, can also bolster energy transport.^{65–67} Nonetheless, this method sets a baseline for future studies to optimize the delocalization of the vibronic Hamiltonian's eigenstates.

The inverse participation ratios depend on the vibronic coupling strengths compared to the vibronic frequencies. To find the basic contours of how the delocalization depends on the coupling, we construct a basic example where the vibronic frequencies are held constant while the coupling terms are multiplied by a scalar variable. Select dependencies are shown in Figure S11, and the full table is presented as Table S2 of the Supporting Information. As the coupling terms are multiplied by a number increasing from 0.25 to 10, the inverse participation ratio of the lowest-energy eigenstate increases from 2.22 to 8.87 in Cy3 and 2.32 to 8.47 in Cy5, suggesting that greater vibronic delocalization can be achieved by increasing the vibronic coupling strength. The delocalization also increases in the second-lowest eigenstates, while the third-lowest eigenstates saturate at the maximum at a multiple of approximately 5 and then decrease again. In principle, this scalar multiple could be achieved by shifting the intermolecular distance within the dimer while preserving the orientations; however, this example is intended as a minimal one to establish that it is possible to obtain substantial vibronic delocalization in principle. In practice, there are many degrees of freedom to search to find the optima, including the bases in the DNA, the choice of chromophores, the positions and orientations, and energy-level characteristics. While these results establish that such optimization can significantly influence the inverse participation ratio, a full investigation of how the vibronic delocalization can be optimized by realistic parameters of molecular systems, and how to achieve this optimization on the lab bench, is the subject of future work.

CONCLUSIONS

Vibronically coupled, DNA-scaffolded Cy3 and Cy5 systems were studied based on their measured and computed optical spectra. The particular focus was on their structures, energetics, and system–environment interactions. The system–environment interactions were initially probed using temperature-dependent spectral measurements. The spectra exhibited line-narrowing by approximately a factor of 2 as the temperature was reduced from room temperature to 78 K. At 78 K, upper HWHM limits of approximately 162 cm^{−1} (Cy3) or 166 cm^{−1} (Cy5) were found for the static inhomogeneous broadening contributions of the 0–0 fluorescence peak. This estimate was further refined by using physical modeling and a genetic algorithm approach, which was able to distinguish the static inhomogeneous broadening contributions from the dynamic contributions. The results obtained were 126 and 135 cm^{−1} for Cy3 and Cy5, respectively. These results indicate that static broadening contributions were the majority contributor to spectral broadening in these systems. This result is relevant for applications that rely on mixing of the electronic states.^{62–64,66,67}

Over a narrower temperature range from room temperature to about 180 K, the fluorescence emissions were observed to increase several fold, most dramatically in the case of Cy5. These results indicate that nonradiative decay processes dominate at higher temperatures but can largely be frozen

out with a relatively mild temperature decrease. For the Cy3 dimer, a fluorescence quantum yield of nearly unity was inferred from the integrated fluorescence spectra. Both the Cy3 and Cy5 dimers displayed small Stokes shifts at 78 K, which is a feature of approaching the temperature-dependent homogeneous broadening limit, as discussed in the Methods Section.

Meanwhile, the vibronic energy structure deduced by the genetic algorithm indicates that delocalization of the lowest-lying eigenstates spans 2–5 vibronic states in the dimers. This is a low-to-moderate delocalized result that could benefit from further optimization. For reference, the excitons (not vibrons) in a photosynthetic pigment–protein complex (the Fenna–Matthews–Olson complex) are delocalized across 1–3 states.²⁸ However, the approach reported here provides a baseline for further optimization in future work. For instance, stronger vibronic coupling was shown to yield greater delocalization of the three lowest eigenstates though it also caused more localization of the higher-wavenumber eigenstates. In practice, many degrees of freedom exist for further optimization that were not explored here, such as the transition dipole orientations, site energies, and scaffold structures. Recent work suggests that the environmental correlations at each site may even be optimized by arranging the chromophore networks into particular spatial patterns, providing another way to control the coherent dynamics and therefore also the broadening characteristics.²⁰ Future studies must be conducted to optimize these properties using the molecular and scaffold characteristics.

ASSOCIATED CONTENT

Supporting Information

The Supporting Information is available free of charge at <https://pubs.acs.org/doi/10.1021/acs.jpca.1c07205>.

DNA scaffolds, PAGE gels, normalized spectra, temperature dependence of spectra, monomer fraction estimates, spectral peak widths, solvent dependence, Hamiltonian parameters, and eigenstate information (PDF)

AUTHOR INFORMATION

Corresponding Author

Joseph S. Melinger — *Electronics Science and Technology Division, Code 6800, U.S. Naval Research Laboratory, Washington, D.C. 20375, United States*; orcid.org/0000-0002-2452-5245; Email: joseph.melinger@nrl.navy.mil

Authors

Brian S. Rolczynski — *Electronics Science and Technology Division, Code 6800, U.S. Naval Research Laboratory, Washington, D.C. 20375, United States*; orcid.org/0000-0002-8783-1266

Sebastián A. Díaz — *Center for Bio/Molecular Science and Engineering, Code 6900, U.S. Naval Research Laboratory, Washington, D.C. 20375, United States*; orcid.org/0000-0002-5568-0512

Young C. Kim — *Materials Science and Technology Division, Code 6300, U.S. Naval Research Laboratory, Washington, D.C. 20375, United States*

Igor L. Medintz — *Center for Bio/Molecular Science and Engineering, Code 6900, U.S. Naval Research Laboratory, Washington, D.C. 20375, United States*; orcid.org/0000-0002-8902-4687

Paul D. Cunningham — Electronics Science and Technology Division, Code 6800, U.S. Naval Research Laboratory, Washington, D.C. 20375, United States; orcid.org/0000-0002-3602-1503

Complete contact information is available at:
<https://pubs.acs.org/10.1021/acs.jpca.1c07205>

Notes

The authors declare no competing financial interest.

ACKNOWLEDGMENTS

The authors thank Professor Bernard Yurke of Boise State University for helpful private discussion. B.S.R. was supported by an ASEE Fellowship from the American Society for Engineering Education. This work was supported by the Naval Research Laboratory Institute for Nanoscience and the Office of Naval Research.

REFERENCES

- (1) Blankenship, R., *Molecular Mechanisms of Photosynthesis*; Wiley: Chichester, 2002.
- (2) Cardona, T.; Sánchez-Baracaldo, P.; Rutherford, A. W.; Larkum, A. W. Early Archean Origin of Photosystem II. *Geobiology* **2019**, *17*, 127–150.
- (3) Cannon, B. L.; Kellis, D. L.; Davis, P. H.; Lee, J.; Kuang, W.; Hughes, W. L.; Graugnard, E.; Yurke, B.; Knowlton, W. B. Excitonic AND Logic Gates on DNA Brick Nanobreadboards. *ACS Photonics* **2015**, *2*, 398–404.
- (4) Cunningham, P. D.; Khachatryan, A.; Buckhout-White, S.; Deschamps, J. R.; Goldman, E. R.; Medintz, I. L.; Melinger, J. S. Resonance Energy Transfer in DNA Duplexes Labeled with Localized Dyes. *J. Phys. Chem. B* **2014**, *118*, 14555–14565.
- (5) Kato, T.; Kashida, H.; Kishida, H.; Yada, H.; Okamoto, H.; Asanuma, H. Development of a Robust Model System of FRET using Base Surrogates Tethering Fluorophores for Strict Control of Their Position and Orientation within DNA Duplex. *J. Am. Chem. Soc.* **2013**, *135*, 741–750.
- (6) Mathur, D.; Kim, Y. C.; Díaz, S. A.; Cunningham, P. D.; Rolczynski, B. S.; Ancona, M. G.; Medintz, I. L.; Melinger, J. S. Can a DNA Origami Structure Constrain the Position and Orientation of an Attached Dye Molecule? *J. Phys. Chem. C* **2021**, *125*, 1509–1522.
- (7) Buckhout-White, S.; Spillmann, C. M.; Algar, W. R.; Khachatryan, A.; Melinger, J. S.; Goldman, E. R.; Ancona, M. G.; Medintz, I. L. Assembling Programmable FRET-based Photonic Networks using Designer DNA Scaffolds. *Nat. Commun.* **2014**, *5*, 5615.
- (8) Castellanos, M. A.; Dodin, A.; Willard, A. P. On the Design of Molecular Excitonic Circuits for Quantum Computing: the Universal Quantum Qates. *Phys. Chem. Chem. Phys.* **2020**, *22*, 3048–3057.
- (9) Orf, G. S.; Saer, R. G.; Niedzwiedzki, D. M.; Zhang, H.; McIntosh, C. L.; Schultz, J. W.; Mirica, L. M.; Blankenship, R. E. Evidence for a Cysteine-Mediated Mechanism of Excitation Energy Regulation in a Photosynthetic Antenna Complex. *Proc. Natl. Acad. Sci. U. S. A.* **2016**, *113*, E4486–E4493.
- (10) Rolczynski, B. S.; Navotnaya, P.; Sussman, H. R.; Engel, G. S. Cysteine-Mediated Mechanism Disrupts Energy Transfer to Prevent Photooxidation. *Proc. Natl. Acad. Sci. U. S. A.* **2016**, *113*, 8562–8564.
- (11) Ishizaki, A.; Fleming, G. R. Quantum Coherence in Photosynthetic Light Harvesting. *Annu. Rev. Condens. Matter Phys.* **2012**, *3*, 333–361.
- (12) Cao, J.; Cogdell, R. J.; Coker, D. F.; Duan, H.-G.; Hauer, J. R.; Kleinekathöfer, U.; Jansen, T. L. C.; Mančal, T. S.; Miller, R. J. D.; Ogilvie, J. P.; Prokhorenko, V. I.; Renger, T.; Tan, H. S.; Tempelaar, R.; Thorwart, M.; Thyryhaug, E.; Westenhoff, S.; Zigmantas, D. Quantum Biology Revisited. *Sci. Adv.* **2020**, *6*, 1–12.
- (13) Fratini, S.; Mayou, D.; Ciuchi, S. The Transient Localization Scenario for Charge Transport in Crystalline Organic Materials. *Adv. Funct. Mater.* **2016**, *26*, 2292–2315.
- (14) Schlosshauer, M., *Decoherence and the Quantum-To-Classical Transition*. 3 ed.; Springer US: 2007; 1–428.
- (15) Scholes, G. D. Limits of Exciton Delocalization in Molecular Aggregates. *Faraday Discuss.* **2020**, *221*, 265–280.
- (16) De Boer, S.; Wiersma, D. A. Optical Dynamics of Exciton and Polariton Formation in Molecular Aggregates. *Chem. Phys.* **1989**, *131*, 135–144.
- (17) Haedler, A. T.; Kreger, K.; Issac, A.; Wittmann, B.; Kivala, M.; Hammer, N.; Köhler, J.; Schmidt, H.-W.; Hildner, R. Long-Range Energy Transport in Single Supramolecular Nanofibres at Room Temperature. *Nature* **2015**, *523*, 196–199.
- (18) Abramavicius, D.; Mukamel, S. Exciton Dynamics in Chromophore Aggregates with Correlated Environment Fluctuations. *J. Chem. Phys.* **2011**, *134*, 174504.
- (19) Rolczynski, B. S.; Zheng, H.; Singh, V. P.; Navotnaya, P.; Ginzburg, A. R.; Caram, J. R.; Ashraf, K.; Gardiner, A. T.; Yeh, S.-H.; Kais, S.; et al. Correlated Protein Environments Drive Quantum Coherence Lifetimes in Photosynthetic Pigment-Protein Complexes. *Chem* **2018**, *4*, 138–149.
- (20) Scholes, G. D. Polaritons and excitons: Hamiltonian Design for Enhanced Coherence. *Proc. R. Soc. A* **2020**, *476*, 20200278–20200228.
- (21) Flanagan, M. L.; Long, P. D.; Dahlberg, P. D.; Rolczynski, B. S.; Massey, S. C.; Engel, G. S. Mutations to R. sphaeroides Reaction Center Perturb Energy Levels and Vibronic Coupling but Not Observed Energy Transfer Rates. *J. Phys. Chem. A* **2016**, *120*, 1479–1487.
- (22) Kringle, L.; Sawaya, N. P. D.; Widom, J.; Adams, C.; Raymer, M. G.; Aspuru-Guzik, A.; Marcus, A. H. Temperature-Dependent Conformations of Cxciton-Coupled Cy3 Dimers in Double-Stranded DNA. *J. Chem. Phys.* **2018**, *148*, 085101–085114.
- (23) Biaggne, A.; Knowlton, W. B.; Yurke, B.; Lee, J.; Li, L. Substituent Effects on the Solubility and Electronic Properties of the Cyanine Dye Cy5: Density Functional and Time-Dependent Density Functional Theory Calculations. *Molecules* **2021**, *26*, 524–539.
- (24) Cannon, B. L.; Kellis, D. L.; Patten, L. K.; Davis, P. H.; Lee, J.; Graugnard, E.; Yurke, B.; Knowlton, W. B. Coherent Exciton Delocalization in a Two-State DNA-Templated Dye Aggregate System. *J. Phys. Chem. A* **2017**, *121*, 6905–6916.
- (25) Cunningham, P. D.; Kim, Y. C.; Díaz, S. A.; Buckhout-White, S.; Mathur, D.; Medintz, I. L.; Melinger, J. S. Optical Properties of Vibronically Coupled Cy3 Dimers on DNA Scaffolds. *J. Phys. Chem. B* **2018**, *122*, 5020–5029.
- (26) Roller, E.-M.; Khorashad, L. K.; Fedoruk, M.; Schreiber, R.; Govorov, A. O.; Liedl, T. DNA-Assembled Nanoparticle Rings Exhibit Electric and Magnetic Resonances at Visible Frequencies. *Nano Lett.* **2015**, *15*, 1368–1373.
- (27) Sissa, C.; Painelli, A.; Terenziani, F.; Trotta, M.; Ragni, R. About the origin of the Large Stokes shift in Aminoalkyl Substituted Heptamethine cyanine Dyes. *Phys. Chem. Chem. Phys.* **2019**, *22*, 129–135.
- (28) Cho, M.; Vaswani, H. M.; Brixner, T.; Stenger, J.; Fleming, G. R. Exciton Analysis in 2D Electronic Spectroscopy. *J. Phys. Chem. B* **2005**, *109*, 10542–10556.
- (29) Wowk, B. Thermodynamic Aspects of Vitrification. *Cryobiology* **2010**, *60*, 11–22.
- (30) Fahy, G. M.; MacFarlane, D. R.; Angell, C. A.; Meryman, H. T. Vitrification as an Approach to Cryopreservation. *Cryobiology* **1984**, *21*, 407–426.
- (31) Philpott, M. R. Theory of the Coupling of Electronic and Vibrational Excitations in Molecular Crystals and Helical Polymers. *J. Chem. Phys.* **1971**, *55*, 2039–2054.
- (32) Karsten, S.; Ivanov, S. D.; Bokarev, S. I.; Kühn, O. Quasi-Classical Approaches to Vibronic Spectra Revisited. *J. Chem. Phys.* **2018**, *148*, 102337.

- (33) Hestand, N. J.; Spano, F. C. Expanded Theory of H- and J-Molecular Aggregates: The Effects of Vibronic Coupling and Intermolecular Charge Transfer. *Chem. Rev.* **2018**, *118*, 7069–7163.
- (34) Kühn, O.; Renger, T.; May, V. Theory of Exciton-Vibrational Dynamics in Molecular Dimers. *Chem. Phys.* **1996**, *204*, 99–114.
- (35) Diehl, F. P.; Roos, C.; Duymaz, A.; Lunkenheimer, B.; Köhn, A.; Basché, T. Emergence of Coherence through Variation of Intermolecular Distances in a Series of Molecular Dimers. *J. Phys. Chem. Lett.* **2014**, *5*, 262–269.
- (36) Schröter, M.; Ivanov, S. D.; Schulze, J.; Polyutov, S. P.; Yan, Y.; Pullerits, T.; Kühn, O. Exciton-Vibrational Coupling in the Dynamics and Spectroscopy of Frenkel Excitons in Molecular Aggregates. *Phys. Rep.* **2015**, *567*, 1–78.
- (37) Kistler, K. A.; Pochas, C. M.; Yamagata, H.; Matsika, S.; Spano, F. C. Absorption, Circular Dichroism, and Photoluminescence in Perylene Diimide Bichromophores: Polarization-Dependent H- and J-Aggregate Behavior. *J. Phys. Chem. B* **2012**, *116*, 77–86.
- (38) Markovitsi, D.; Germain, A.; Millie, P.; Lecuyer, P.; Gallos, L. K.; Argyrakakis, P.; Bengs, H.; Ringsdorf, H. Triphenylene Columnar Liquid Crystals: Excited States and Energy Transfer. *J. Phys. Chem.* **1995**, *99*, 1005–1017.
- (39) de Jong, M.; Seijo, L.; Meijerink, A.; Rabouw, F. T. Resolving the Ambiguity in the Relation between Stokes Shift and Huang–Rhys Parameter. *Phys. Chem. Chem. Phys.* **2015**, *17*, 16959–16969.
- (40) Wang, J.; Wolf, R. M.; Caldwell, J. W.; Kollman, P. A.; Case, D. A. Development and Testing of a General Amber Force Field. *J. Comput. Chem.* **2004**, *25*, 1157–1174.
- (41) Mukamel, S., *Nonlinear Optical Spectroscopy*; Oxford U. Press: Oxford, 1995.
- (42) Renger, T.; Marcus, R. A. On the Relation of Protein Dynamics and Exciton Relaxation in Pigment–Protein Complexes: An Estimation of the Spectral Density and a Theory for the Calculation of Optical Spectra. *J. Chem. Phys.* **2002**, *116*, 9997–10019.
- (43) Schellman, J. A. Circular Dichroism and Optical Rotation. *Chem. Rev.* **1975**, *75*, 323–331.
- (44) Sivanandam, S. N.; Deepa, S. N., *Introduction to Genetic Algorithms*; Springer: Berlin, 2008; 1–453.
- (45) Kalra, S.; Rahnamayan, S.; Deb, K. In 2017 IEEE Congress on Evolutionary Computation (CEC), *IEEE CEC, Donostia, Spain, June 5–8, 2017*; IEEE: Piscataway, 2017, 2328–2337.
- (46) Sohail, S. H.; Otto, J. P.; Cunningham, P. D.; Kim, Y. C.; Wood, R. E.; Allodi, M. A.; Higgins, J. S.; Melinger, J. S.; Engel, G. S. DNA Scaffold Supports Long-Lived Vibronic Coherence in an Indodicarbocyanine (Cy5) Dimer. *Chem. Sci.* **2020**, *11*, 8546–8557.
- (47) Polyutov, S.; Kühn, O.; Pullerits, T. N. Exciton-Vibrational Coupling in Molecular Aggregates: Electronic Versus Vibronic Dimer. *Chem. Phys.* **2012**, *394*, 21–28.
- (48) Mazuski, R. J.; Díaz, S. A.; Wood, R. E.; Lloyd, L. T.; Klein, W. P.; Mathur, D.; Melinger, J. S.; Engel, G. S.; Medintz, I. L. Ultrafast Excitation Transfer in Cy5 DNA Photonic Wires Displays Dye Conjugation and Excitation Energy Dependency. *J. Phys. Chem. Lett.* **2020**, *11*, 4163–4172.
- (49) Brooker, L. G. S.; White, F. L.; Sprague, R. H.; Dent, S. G., Jr.; van Zandt, G. Steric Hindrance to Planarity in Dye Molecules. *Chem. Rev.* **1947**, *41*, 325–351.
- (50) Lee, H.; Berezin, M. Y.; Henary, M.; Strekowski, L.; Achilefu, S. Fluorescence Lifetime Properties of Near-Infrared Cyanine Dyes in Relation to their Structures. *J. Photochem. Photobiol. A: Chem.* **2008**, *200*, 438–444.
- (51) Sibbett, W.; Taylor, J. R.; Welford, D. Substituent and Environmental Effects on the Picosecond Lifetimes of the Polymethine Cyanine Dyes. *IEEE J. Quantum Electron.* **1981**, *17*, 500–509.
- (52) Huff, J. S.; Davis, P. H.; Christy, A.; Kellis, D. L.; Kandadai, N.; Toa, Z. S. D.; Scholes, G. D.; Yurke, B.; Knowlton, W. B.; Pensack, R. D. DNA-Templated Aggregates of Strongly Coupled Cyanine Dyes: Nonradiative Decay Governs Exciton Lifetimes. *J. Phys. Chem. Lett.* **2019**, *10*, 2386–2392.
- (53) Cunningham, P. D.; Díaz, S. A.; Yurke, B.; Medintz, I. L.; Melinger, J. S. Delocalized Two-Exciton States in DNA Scaffolded Cyanine Dimers. *J. Phys. Chem. B* **2020**, *124*, 8042–8049.
- (54) Knapp, E. W. Lineshapes of Molecular Aggregates. Exchange Narrowing and Intersite Correlation. *Chem. Phys.* **1984**, *85*, 73–82.
- (55) Scheblykin, I. G.; Sliusarenko, O. Y.; Lepnev, L. S.; Vitukhnovsky, A. G.; Van der Auweraer, M. Excitons in Molecular Aggregates of 3,3'-Bis-[3-sulfopropyl]-5,5'-dichloro-9-ethylthiacarbocyanine (THIATS): Temperature Dependent Properties. *J. Phys. Chem. B* **2001**, *105*, 4636–4646.
- (56) Kaiser, T. E.; Stepanenko, V.; Würthner, F. Fluorescent J-Aggregates of Core-Substituted Perylene Bisimides: Studies on Structure–Property Relationship, Nucleation–Elongation Mechanism, and Sergeants-and-Soldiers Principle. *J. Am. Chem. Soc.* **2009**, *131*, 6719–6732.
- (57) Rolczynski, B. S.; Yeh, S.-H.; Navotnaya, P.; Lloyd, L. T.; Ginzburg, A. R.; Zheng, H.; Allodi, M. A.; Otto, J. P.; Ashraf, K.; Gardiner, A. T.; et al. Time-Domain Line-Shape Analysis from 2D Spectroscopy to Precisely Determine Hamiltonian Parameters for a Photosynthetic Complex. *J. Phys. Chem. B* **2021**, *125*, 2812–2820.
- (58) Connolly, J. S.; Samuel, E. B.; Janzen, A. F. Effects of Solvent on the Fluorescence Properties of Bacteriochlorophyll a. *Photochem. Photobiol.* **1982**, *36*, 565–574.
- (59) Fidler, H.; Knoester, J.; Wiersma, D. A. Superradiant Emission and Optical Dephasing in J-aggregates. *Chem. Phys. Lett.* **1990**, *171*, 529–536.
- (60) Nagasawa, Y. Ultrafast Photon Echo Experiments in Condensed Phase: Detection of Solvation Dynamics, Coherent Wavepacket Motions and Static Inhomogeneity. *J. Photochem. Photobiol. C* **2011**, *12*, 31–45.
- (61) Spano, F. C. The Spectral Signatures of Frenkel Polarons in H- and J-Aggregates. *Acc. Chem. Res.* **2010**, *43*, 429–439.
- (62) Nielson, M. A.; Chuang, I. L., *Quantum Computation and Quantum Information*; Cambridge U. Press: New York, 2010, 1–704.
- (63) Wendin, G. Quantum Information Processing with Superconducting Circuits: A Review. *Rep. Prog. Phys.* **2017**, *80*, 106001–106051.
- (64) Biamonte, J.; Wittek, P.; Pancotti, N.; Rebentrost, P.; Wiebe, N.; Lloyd, S. Quantum Machine Learning. *Nature* **2017**, *549*, 195–202.
- (65) Plenio, M. B.; Huelga, S. F. Dephasing-Assisted Transport: Quantum Networks and Biomolecules. *New J. Phys.* **2008**, *10*, No. 113019.
- (66) Rebentrost, P.; Mohseni, M.; Kassal, I.; Lloyd, S.; Aspuru-Guzik, A. Environment-Assisted Quantum Transport. *New J. Phys.* **2009**, *11*, No. 033003.
- (67) Moix, J. M.; Khasin, M.; Cao, J. Coherent Quantum Transport in Disordered Systems: I. The Influence of Dephasing on the Transport Properties and Absorption Spectra on One-Dimensional Systems. *New J. Phys.* **2013**, *15*, 085010–085022.